

Interface-specific x-ray phase retrieval tomography of complex biological organs

This article has been downloaded from IOPscience. Please scroll down to see the full text article.

2011 Phys. Med. Biol. 56 7353

(<http://iopscience.iop.org/0031-9155/56/23/002>)

View [the table of contents for this issue](#), or go to the [journal homepage](#) for more

Download details:

IP Address: 130.194.20.173

The article was downloaded on 29/12/2011 at 12:56

Please note that [terms and conditions apply](#).

Interface-specific x-ray phase retrieval tomography of complex biological organs

M A Beltran¹, D M Paganin¹, K K W Siu^{1,2,3}, A Fouras⁴, S B Hooper⁵,
D H Reser⁶ and M J Kitchen¹

¹ School of Physics, Monash University, Victoria 3800, Australia

² Monash Biomedical Imaging, Monash University, Victoria 3800, Australia

³ Australian Synchrotron, Victoria 3168, Australia

⁴ Division of Biological Engineering, Monash University, Victoria 3800, Australia

⁵ The Ritchie Centre, Monash Institute of Medical Research, Monash University, Victoria 3800, Australia

⁶ Department of Physiology, Monash University, Victoria 3800, Australia

E-mail: Marcus.Kitchen@monash.edu


Received 31 May 2011, in final form 29 September 2011

Published 2 November 2011

Online at stacks.iop.org/PMB/56/7353

Abstract

We demonstrate interface-specific propagation-based x-ray phase retrieval tomography of the thorax and brain of small animals. Our method utilizes a single propagation-based x-ray phase-contrast image per projection, under the assumptions of (i) partially coherent paraxial radiation, (ii) a static object whose refractive indices take on one of a series of distinct values at each point in space and (iii) the projection approximation. For the biological samples used here, there was a 9–200 fold improvement in the signal-to-noise ratio of the phase-retrieved tomograms over the conventional attenuation-contrast signal. The ability to ‘digitally dissect’ a biological specimen, using only a single phase-contrast image per projection, will be useful for low-dose high-spatial-resolution biomedical imaging of form and biological function in both healthy and diseased tissue.

 Online supplementary data available from stacks.iop.org/PMB/56/7353/mmedia

(Some figures in this article are in colour only in the electronic version)

1. Introduction

Phase-contrast imaging is any optical technique whereby phase changes imparted by an object to the incident coherent, or partially coherent, radiation are rendered visible in the

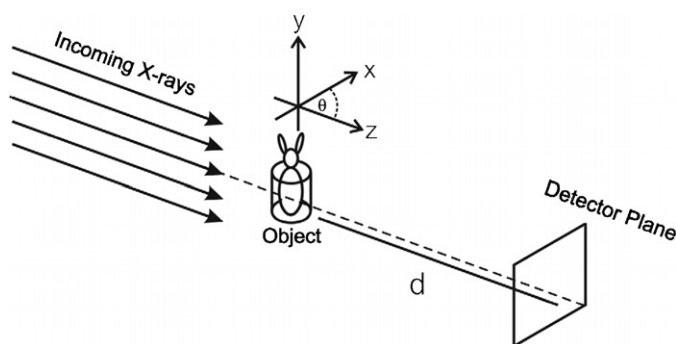


Figure 1. Experimental setup illustrating the geometry for propagation-based x-ray phase retrieval tomography, using a single view per projection.

measured intensity. Phase-contrast x-ray computed tomography (CT) can provide images with better signal-to-noise ratio (SNR) than conventional x-ray absorption-contrast CT for imaging samples in three dimensions that exhibit weak absorption, such as biological specimens (Mayo *et al* 2003, Arhatari *et al* 2010, Beltran *et al* 2010). The most common phase-contrast techniques are x-ray interferometry (Momose *et al* 1996), x-ray diffraction grating methods (Pfeiffer *et al* 2007), analyser-based phase-contrast imaging (ABI) (Förster *et al* 1980) and propagation-based phase-contrast imaging (PBI) (Snigirev *et al* 1995).

The technique used in the present paper is PBI. Unlike the other methods mentioned above, PBI does not require any additional optical elements between the sample and detector. In PBI, the act of free-space propagation—from the exit surface of a sample illuminated by a spatially coherent source to the surface of a two-dimensional position-sensitive detector—renders visible the transverse phase shifts imparted by the sample upon the illuminating radiation (Snigirev *et al* 1995, Wilkins *et al* 1996, Cloetens *et al* 1996, 1999, Pogany *et al* 1997) (see figure 1).

With PBI, visualization of poorly absorbing features in a sample can significantly improve in comparison to absorption-contrast alone. However, quantitative information about the phase cannot be directly inferred from the raw PBI images. In order to extract phase information, phase retrieval methods may be employed. Numerous phase retrieval algorithms that require intensity-only measurements have been developed to yield the projected phase and absorption information of an object (Teague 1983, Gureyev and Nugent 1996, 1997, Paganin and Nugent 1998, Cloetens *et al* 1999, Guigay *et al* 2007). Despite their success, many of these algorithms require the acquisition of multiple images per tomographic projection, or impose significant restrictions on the object under study (e.g., it must provide weak or no attenuation contrast). When it comes to using ionizing radiation to image biological specimens, taking more than one image per projection will induce a higher radiation dose, which can be detrimental. Dose consideration is particularly important for *in vivo* studies, and thus methods requiring large numbers of projections are of limited use for biomedical applications.

A significant amount of work has been done on the question of tomographic reconstruction using x-ray PBI. Key works include, but are not limited to, (i) Cloetens *et al* (1997), who reconstructed raw x-ray propagation-based phase-contrast data using filtered backprojection to give an edge-enhanced three-dimensional representation of the object; (ii) Cloetens *et al* (1999) on ‘holotomography’, which utilized through-focal-series phase retrieval methods originally developed in the field of electron microscopy, in the context of quantitative

x-ray phase-contrast tomography; (iii) x-ray phase-contrast tomography which incorporated the transport-of-intensity equation (Teague 1983) for the phase retrieval analysis of each projection prior to three-dimensional reconstruction (Mayo *et al* 2003, McMahon *et al* 2003); (iv) Bronnikov's merging of the phase retrieval and tomography steps into a single algorithm for the case of a transparent object (Bronnikov 2002), together with the generalization of this work by Gureyev *et al* (2006); (v) extension of Wolf's work on diffraction tomography (Wolf 1969), in the context of x-ray phase contrast, by Anastasio and Pan (2000); (vi) Myers *et al* (2010) on phase retrieval tomography of few-material objects using a limited number of views, together with work on gradient-sparse objects by Sidky *et al* (2010); and (vii) local phase-contrast tomography (Anastasio *et al* 2004, Shi *et al* 2005, Gureyev *et al* 2007). For a balanced overview of the contemporary state of the art in x-ray phase-contrast tomography, we refer to the proceedings of the *Conference on Developments in X-Ray Tomography VII*, edited by Stock (2010).

As a key ingredient of the work presented here, Paganin *et al* (2002) developed a phase retrieval algorithm that only requires a single PBI image per projection. Their algorithm was derived under the strong assumption that the sample be comprised of a single homogeneous material that is imaged under paraxial coherent x-ray illumination. It has proven to be very robust under the influence of noise and has also been utilized in a number of PBI tomographic studies (Mayo *et al* 2003, Gureyev *et al* 2006, Arhatari *et al* 2010). The work of Paganin *et al* (2002) was extended by Beltran *et al* (2010) to enable interface-specific phase retrieval tomography to be performed on samples composed of a finite number of materials which are spatially quantized, under the assumptions that (i) each material type within the sample may be adequately approximated by a single complex refractive index; (ii) the complex refractive index of each distinct material has a distinct value; (iii) no more than two interfaces can be in direct contact at any given location. While any real sample will have variations in homogeneity within each given material, this was seen to have a minimal effect on the tomographic reconstruction, both in the previously reported work by Beltran *et al* (2010) and in the new work reported in the present paper. In this context, note also that the previously mentioned variations in homogeneity are often within the uncertainties of the real and imaginary parts of the complex refractive index, for biological samples at diagnostic x-ray energies. Importantly, this technique retains the salient feature of requiring only a single phase-contrast image per projection. As a proof of principle, the authors tested their technique on PBI tomographic experimental data taken of a simple test phantom which contained three different materials. Each material was quantitatively reconstructed separately and spliced together into a complete reconstruction (Beltran *et al* 2010).

In this investigation, we apply the technique developed by Beltran *et al* (2010) to carry out interface-specific phase retrieval tomography, without using any chemical contrast enhancements, on complex biological organs including the thorax of a newborn New Zealand white rabbit pup and the excised brain of an adult Sprague Dawley rat. Our aim was to determine whether our single-image phase retrieval technique could be applied to complex structures and to measure the gain in the SNR of the reconstructed images over conventional CT.

The outline of our paper is as follows. Section 2 reviews the underlying theory of the method developed by Beltran *et al* (2010), for interface-specific phase retrieval x-ray tomography of objects whose refractive indices take on one of a series of discrete values. Section 3 describes the setup and procedures used for the experimental implementation on two complex biological samples, namely rabbit lung and rat brain tissue. Section 4 illustrates the results achieved using interface-specific tomography. We provide discussion for future work in section 5 and conclude with section 6.

2. Theory: phase retrieval for a single- and two-material sample

Underpinning our phase retrieval method is the algorithm developed by Paganin *et al* (2002), which requires only a single two-dimensional PBI image per tomographic projection. Its derivation was based on the transport of intensity equation (Teague 1983) for a paraxial monochromatic wavefield together with the assumption that the imaged object is comprised of a single homogeneous material. The algorithm has proven to be computationally efficient and robust under the presence of noise in a number of subsequent studies (e.g., Mayo *et al* 2003, Paganin *et al* 2004, Turner *et al* 2004, Kitchen *et al* 2008, Irvine *et al* 2008, Beltran *et al* 2010, Stevenson *et al* 2010).

For an object that is composed of material ‘1’ which has complex refractive index $n = 1 - \delta_1 + i\beta_1$, an argument combining Teague’s transport of intensity equation (Teague 1983) and Beer’s law of attenuation implies that the projected thickness can be calculated from the measured intensity using (Paganin *et al* 2002):

$$T_1(\mathbf{r}_\perp) = -\frac{1}{\mu_1} \log_e \left(\mathbf{F}^{-1} \left\{ \frac{1}{(d\delta_1/\mu_1)\mathbf{k}_\perp^2 + 1} \mathbf{F} \left\{ \frac{I(\mathbf{r}_\perp, z = d)}{I_0} \right\} \right\} \right). \quad (1)$$

Here, \mathbf{F} and \mathbf{F}^{-1} respectively represent the forward and inverse Fourier transforms with respect to $\mathbf{r}_\perp = (x, y)$, $\mathbf{k}_\perp = (k_x, k_y)$ are the Fourier coordinates dual to \mathbf{r}_\perp , λ is the wavelength of the radiation, μ_1 is the linear coefficient related to the imaginary part of the complex refractive index via $\mu_1 = 4\pi\beta_1/\lambda$, $I(\mathbf{r}_\perp, z = d)$ is the intensity of the PBI image measured at a propagation distance d along the z -direction from the sample’s exit surface plane to the detector plane and I_0 is the incident intensity. Equation (1) is only valid for the near-field approximation, that is, the propagation distance d is small enough such that the Fresnel number $N_F = \ell^2/\lambda d$ (where ℓ is the characteristic transverse length scale of the object’s exit surface wave-field) is much larger than unity (Saleh and Teich 1991). Further assumptions, required for the validity of the above equation, include (i) the projection approximation, (ii) normally incident coherent plane-wave illumination and (iii) paraxiality of the exit-surface wavefield.

When applied to spatially quantized objects, whose three-dimensional complex refractive index takes on one of a series of distinct values, equation (1) will of course not correctly reconstruct the projected thickness of a given specific material. However, this problem can be alleviated when relative differences for μ and δ , corresponding to any pair of materials (i.e. a material–material interface), are incorporated into the equation. Thus, when a tilt series (i.e. a tomographic dataset of sample angular orientations) of the resulting retrieved ‘projected thickness’ maps are tomographically reconstructed, the reconstruction corresponding to the specified interface will be accurately obtained, superposed with a three-dimensional signal corresponding to the ‘other’ material interfaces that only locally pollute the boundary of the region containing the pair of materials of interest. This method was implemented for quantized ternary samples (containing two homogeneous materials plus voids) by Beltran *et al* (2010), for which we provide a brief review of the relevant theory and approximations.

If a medium of interest denoted by ‘ j ’ is embedded within a medium denoted as ‘1’, their respective projected thicknesses are given by $T_j(\mathbf{r}_\perp)$ and $T_1(\mathbf{r}_\perp)$. $T_j(\mathbf{r}_\perp)$ can then be calculated using (Beltran *et al* 2010):

$$T_j(\mathbf{r}_\perp) = -\frac{1}{\mu_j - \mu_1} \log_e \left(\mathbf{F}^{-1} \left\{ \frac{1}{[d(\delta_j - \delta_1)/(\mu_j - \mu_1)]\mathbf{k}_\perp^2 + 1} \mathbf{F} \left\{ \frac{I(\mathbf{r}_\perp, z = d)}{I_0 \exp[-\mu_1 A(\mathbf{r}_\perp)]} \right\} \right\} \right) \quad (2)$$

for each projection; one can then run the resulting thickness maps through a conventional tomographic reconstruction algorithm, such as filtered backprojection. For the same reasons as

mentioned in the previous paragraph, equation (2) will not reconstruct the projected thickness of each member of the tilt series, but it will correctly reconstruct the three-dimensional distribution of interfaces between a given pair of distinct materials, with only local pollution of the nature previously described. Note also that equation (2) was derived under the assumption that the phase gradients imparted on the incident wavefield due to the object's total projected thickness, $A(\mathbf{r}_\perp)$, are slowly varying. Utilizing equation (2) requires *a priori* knowledge of $A(\mathbf{r}_\perp)$ in addition to the values δ_j , δ_1 and μ_j , μ_1 corresponding to the different materials in the object. In practice, to generate the function $A(\mathbf{r}_\perp)$ to reconstruct an object of a high degree of complexity, and which contains no internal voids, one can use techniques such as laser profilometry (Myers *et al* 2008a). In the case of tomographic studies, a more practical approach to obtain $A(\mathbf{r}_\perp)$ for each projection angle can be used. By applying equation (1) to each PBI image, the encasing material can first be tomographically reconstructed. Then, both internal and external voids can be located by computationally searching for a predefined threshold in each slice of the reconstructed volume, and thus $A(\mathbf{r}_\perp)$ may then be calculated for each projection angle. We also mention that for point source illumination, image magnification in equations (1) and (2) needs to be accounted for (see e.g., Kitchen *et al* 2008).

A benefit of equations (1) and (2) is their high degree of numerical stability, due to the fact that the images are smoothed by a low-pass Fourier space filter during the initial part of the phase retrieval process. This smoothing, via the phase-retrieval integral transform represented by equations (1) and (2), leads to a concomitant reduction in high-frequency noise in the images, thereby improving the SNR without blurring the boundaries between interfaces. This gain in the SNR can potentially be traded against an equivalent x-ray dose reduction.

3. Method

3.1. Image acquisition

High-resolution x-ray phase-contrast images were acquired in hutch 3 of beamline 20B2 at the SPring-8 synchrotron radiation source, Japan (Goto *et al* 2001). The large source-to-object distance (~ 210 m) and the Si(1 1 1) double-crystal monochromator provided a near planar x-ray beam. We used 24 keV x-rays to provide strong phase and attenuation contrast of the biological specimens used here (see Kitchen *et al* 2008, Beltran *et al* 2010), which included the thorax of a newborn New Zealand white rabbit pup and the excised brain of an adult Sprague Dawley rat. The beam size was collimated to be approximately 30 mm wide and 30 mm high, which was large enough to illuminate each sample. A 4000×2672 pixel Hamamatsu CCD camera (C9300-124F) with a 1.8:1 ratio fibre optic taper, having an effective pixel size of 16.2 μm , was used to collect the tomographic tilt series of propagation-based x-ray phase-contrast images (see figure 1).

For imaging the rabbit pup thorax, the detector was positioned a distance $d = 50$ cm from the object. This relatively small sample-to-detector propagation distance was sufficient to render visible strong phase-contrast fringes from the air–tissue interfaces within the lung at this energy (see, e.g., Suzuki *et al* 2002, Beltran *et al* 2010). A total of 1500 projections were collected over 180° of rotation, with each having an exposure time of 250 ms. Flat field images (with no object in the beam) were recorded at the start and end of each scan to normalize the image intensity. Dark field images were also collected to correct for the detector's dark current offset.

The same setup was used for imaging the rat brain as for the rabbit pup thorax with the exception of the object-to-detector distance, which was set to 5.0 m. A large propagation distance was required to increase the phase contrast between the materials within the sample

Table 1. Values of δ and μ at 24 keV x-rays for water (soft-tissue equivalent) and cortical bone tissue. These were calculated using the NIST database⁷.

Material	$\delta (\times 10^{-7})$	$\mu (\text{m}^{-1})$
Water (lung tissue equivalent)	3.992	54.9
Bone tissue	7.145	461.1

Table 2. Values of δ and μ at 24 keV x-rays for grey/white matter and agar. These were calculated using the NIST database⁷.

Material	$\delta (\times 10^{-7})$	$\mu (\text{m}^{-1})$
Grey/white matter	4.842	56.3
Agar	3.432	40.2

due to the highly similar refractive indices of the materials (namely grey and white brain matter) within the sample. A total of 1800 tomographic projections were acquired with an exposure time of 2.5 s each.

We note that the large number of projections used here is required for adequate sampling of the tomographic reconstruction, to adequately resolve the phase-contrast fringes which typically have maxima separated by 50–100 μm . Although a considerably lower dose could be achieved using larger pixels with fewer projections, we chose to maximize the phase sensitivity of these applications to take advantage of the high resolution of the camera. The exposure time for the thorax was kept short relative to that of the brain in order to minimize potential motion artefacts introduced by movement of the tissues during the scan.

3.2. Image processing

For the selected energy (24 keV), the δ and μ values for lung tissue and cortical bone are listed in table 1. The δ and μ values considered to be present in the agar-embedded brain sample are listed in table 2. According to the NIST database (<http://www.nist.gov/index.html>), grey and white matter (the main tissue types present in the brain) are virtually identical in reference to diagnostic energy x-ray interactions and are herein treated as identical. We justify this statement by reference to equations (1) and (2) where we see that it is the ratio of the real and imaginary components of the refractive indices, or the difference ratio (see equation (2)), that is important for the Fourier filtering by the phase retrieval algorithms. Figure 2 illustrates this point by comparing the four Fourier-space filters used in this research. Distinct differences can be seen for the lung tissue/air interface filter against those of the brain tissue/agar and bone/lung tissue interfaces. Remarkably, the agar/air filter is almost identical to the brain tissue/agar filter despite the interfaces having very different density gradients, which arises because the ratio of δ to μ is nearly identical for brain tissue and agar (see table 2). Therefore, either filter (equation (1) or (2)) can be applied with essentially the same results.

Since equations (1) and (2) involve ratios of δ and μ , concerns regarding sample inhomogeneity can be partly allayed. Both δ and μ are proportional to the density of a given material; hence, their ratio in equation (1) will be independent of changes in density for a given material. The same holds true for equation (2) when the density of material ‘ j ’ and that

⁷ <http://www.nist.gov/index.html> (accessed 4 April and 10 November 2010).

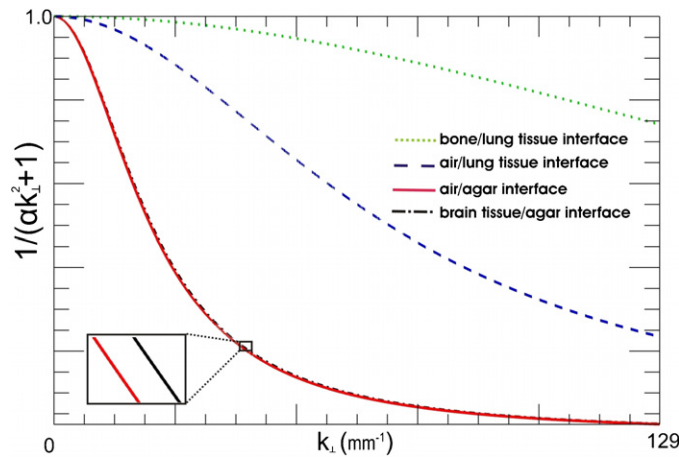


Figure 2. Fourier filters of the form $1/(\alpha k_{\perp}^2 + 1)$ for different ratios of $\alpha = d\delta/\mu$ or $\alpha = d\Delta\delta/\Delta\mu$ (see equations (1) and (2)). The dashed line corresponds to the ratio used for the air/lung tissue interface, $\alpha = d\delta_{\text{water}}/\mu_{\text{water}}$ with $d = 50$ cm. The dotted line corresponds to the ratio used for the bone/lung tissue interface, $\alpha = d(\delta_{\text{bone}} - \delta_{\text{water}})/(\mu_{\text{bone}} - \mu_{\text{water}})$ with $d = 50$ cm. The solid line corresponds to the ratio used for the air/agar interface, $\alpha = d\delta_{\text{agar}}/\mu_{\text{agar}}$, with $d = 5$ m, and the dashed-dotted line corresponds to the ratio used for the brain tissue (grey/white matter; denoted 'gw')/agar interface, $\alpha = d(\delta_{\text{gw}} - \delta_{\text{agar}})/(\mu_{\text{gw}} - \mu_{\text{agar}})$ with $d = 5$ m. The magnified inset is used to illustrate the minute difference between filters for brain tissue/agar and air/agar, respectively.

of material '1' are equal. Moreover, variations in density of a few per cent of either material will typically have little effect on the shape of the filter in equation (2). It is therefore a valid approximation to employ a single filter for a given interface despite small density variations in inhomogeneous samples.

3.3. Animal procedures

All animal procedures were approved by the Monash University Animal Ethics Committee and the SPRing-8 Animal Care and Use Committee. A pregnant New Zealand white rabbit at 31 days of gestation was anaesthetized by intravenous injection of propofol (Rapinivet; 12 mg kg^{-1} bolus, 40 mg h^{-1} infusion). The pup was delivered by caesarean section and then humanely killed via anaesthetic overdose. Following death, an endotracheal tube was inserted via a tracheotomy into the mid-cervical trachea and connected to a custom-designed ventilator (Kitchen *et al* 2010). The pup was placed in a water-filled cylindrical plethysmograph made of Perspex. The head of the pup was located outside the chamber and a thin rubber diaphragm formed a seal around its neck. Once correctly placed in the plethysmograph, the lungs were inflated with air and inflation was maintained by the application of a constant airway pressure of $25 \text{ cmH}_2\text{O}$, as was required to keep the terminal airways inflated.

The rat was humanely killed via an overdose of sodium pentothal (100 mg/kg , i.p.) and then transcardially perfused with heparinized 0.1 M phosphate buffered saline (PBS) followed by 4% paraformaldehyde (PFA) in 0.1 M PBS. The brain was carefully removed from the skull and postfixed overnight in 4% PFA/ 0.1 M PBS. The brain was then serially dehydrated in increasing concentrations of sucrose (up to 30%) in 4% PFA. The fixed brain was next suspended inside a 2.6 cm diameter plastic specimen container containing warm 2% gel agar

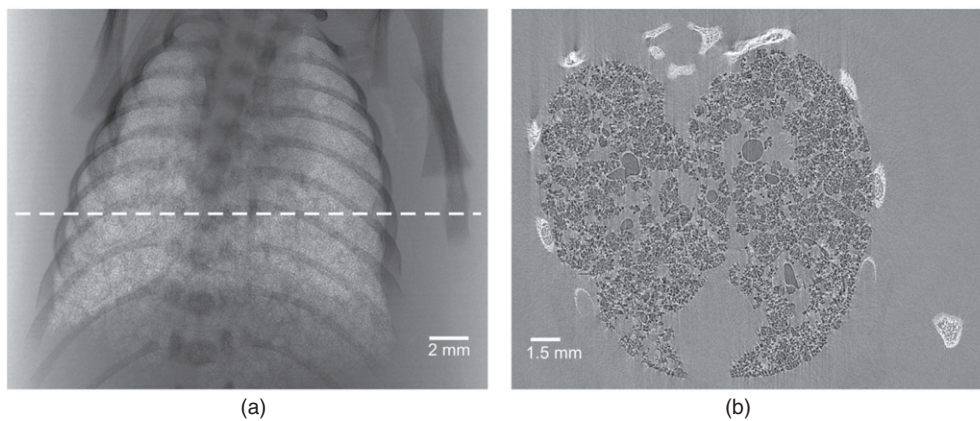


Figure 3. (a) Propagation-based x-ray phase-contrast image of the lungs of a preterm rabbit pup. X-ray energy = 24 keV, propagation distance = 50 cm. (b) Tomographic reconstruction of a single slice (see the dashed line in (a)) from the raw phase-contrast images utilizing filtered backprojection.

diluted with 4% PFA. After the agar hardened, the container was refrigerated until imaging. After synchrotron imaging was complete, the brain was extracted from the agar and sectioned in the coronal plane (50 μm thickness) using a cryostat. Alternating brain sections were stained for Nissl substance (which densely stains the rough endoplasmic reticulum in neuronal cell bodies) and used to locate anatomical landmarks in the propagation-based x-ray phase-contrast images. Anatomical localization was performed with the aid of the stereotaxic atlas of Pellegrino *et al* (1979).

4. Results and discussion

4.1. Chest imaging

A single PBI image of the tomographic data set is shown in figure 3(a). Even with the relatively small object-to-detector distance, the bulk of the lung tissue is rendered visible as a speckled intensity pattern as a result of multiple refraction of the x-ray beam through minor airways that overlap in projection (Kitchen *et al* 2004).

By applying filtered backprojection (Kak and Slaney 1988) using a ramp (Ram-Lak) filter directly to the phase-contrast images, without performing phase retrieval (Cloetens *et al* 1997), we obtain a qualitative reconstruction of the thorax as shown in figure 3(b). Here, the phase-contrast fringes formed at the edges between the interfaces (*i.e.* air/lung and bone/lung tissues) are seen in the reconstruction as residual phase-contrast fringes in the tomogram. We note that slight motion artefacts are also evident due to difficulties in keeping the object stationary for the ~ 7 min of scan time. The phase contrast can aid the visualization of features such as the major airways by highlighting their boundaries. However, the edge enhancement can obscure finer features and restricts quantitative analysis of the tissue morphology (Suzuki *et al* 2002). To perform interface-specific phase retrieval tomography, we apply equations (1) and (2) to each tomographic image followed by filtered backprojection. Depending on which interface one wishes to focus on, the corresponding δ and μ or $\Delta\delta = \delta_2 - \delta_1$ and $\Delta\mu = \mu_2 - \mu_1$ are input into equations (1) and (2), respectively. Here we denote $j = 2$ as the bone/lung tissue interface.

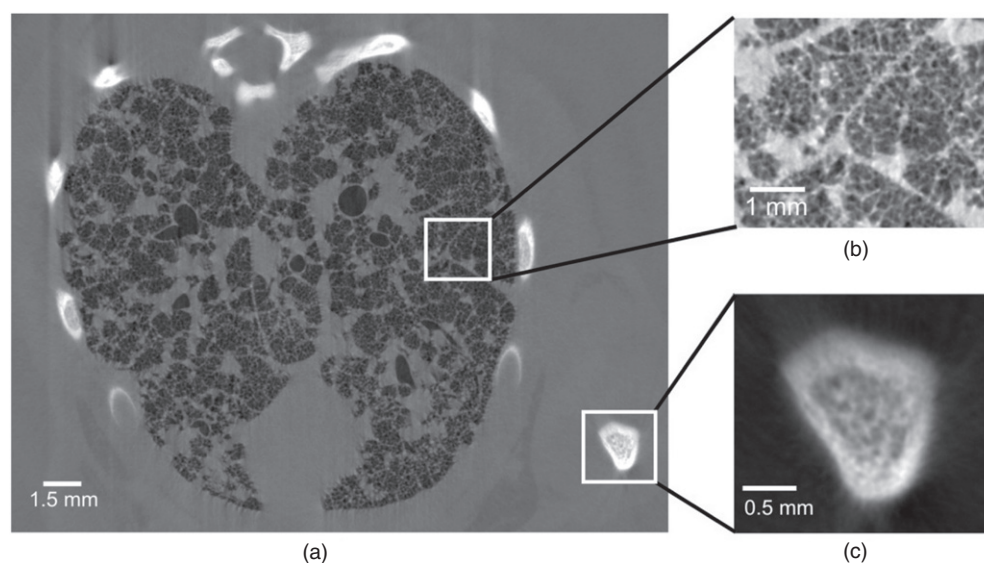


Figure 4. (a) Interface-specific tomographic reconstruction of a preterm rabbit pup thorax, focusing on the air/lung tissue interface. (b) Magnified section of (a) to aid visibility of the terminal airways. (c) Magnified section of (a) in which the bone/lung tissue interface appears blurred as a result of the chosen phase retrieval filter.

In our analysis, we consider lung tissue to be the encasing material. Therefore, to focus in on the air/lung tissue interface, we apply equation (1) to each tomographic image. Here, the δ and μ values for water were inserted into equation (1) as soft tissues and water have similar refractive and absorptive properties at the selected x-ray energy (Kitchen *et al* 2008). A tomographic reconstruction that focuses on the air/lung tissue interface is shown in figure 4(a). This image illustrates that the phase-contrast fringes have been removed, leaving the air/lung tissue interfaces sharply reconstructed, while we can also see that the bone/lung tissue interface has been locally blurred as a result of incorrect choices of δ and μ in the phase retrieval process, which contaminates the local vicinity surrounding this interface (Beltran *et al* 2010). Figure 4(b) shows a zoomed-in region of figure 4(a) in which individual terminal airways (alveoli) are clearly visible.

An important benefit of the phase-retrieved reconstruction (figure 4) is the dramatically improved SNR over the raw tomographic dataset (figure 3(b)). Using three 50×50 pixel regions containing soft tissue only, an SNR of 30 ± 6 (mean \pm standard deviation) was calculated. By comparison, the same area in the raw reconstruction yielded just 1.8 ± 0.3 . Here, we used the formula $\text{SNR} = \tilde{\mu}/\sigma$, where $\tilde{\mu}$ is the mean signal and σ is the standard deviation of voxels in the subarray. However, since no pure absorption-contrast image could be collected due to the finite object-to-detector distance, the latter SNR value was calculated in a region of figure 3 where only absorption-contrast signal exists (i.e. away from residual phase-contrast fringes). Thus, we found an improvement in the soft-tissue SNR of 16 ± 4 fold over absorption contrast for our particular experimental setup. This same improvement in the SNR was also observed (within uncertainties) in the large airspaces (bronchioles). It is not surprising that the noise was so heavily reduced since the phase retrieval algorithms naturally suppress the high-frequency noise.

Employing phase contrast with an appropriate phase retrieval algorithm has enabled us to clearly visualize the terminal airways. Whilst similar data may have been obtained from absorption-contrast tomography, for instance by decreasing the average energy to increase the soft-tissue absorption contrast, the corresponding dose increase would be prohibitive. This has important implications for studying the health of the lungs and other organs. Emphysema, for example, is a disease of the distal airways that is characterized by the loss of alveolar structures. The ability to clearly observe these fine structures could lead to improved diagnosis of early lung disease. We have used this dataset to measure the range of alveolar dimensions found within this animal. The diameters of the alveoli were measured to be between 109 and 162 μm , which is consistent with the previously measured values found in a rabbit pup model (Hooper *et al* 2007). We further demonstrate the fidelity of the reconstruction in the online supplementary movie (available at stacks.iop.org/PMB/56/7353/mmedia) that takes us into the airway tree of the pup, with remarkable clarity all the way to the terminal airsacs (alveoli). This movie was made using commercial software (Amira v 5.2, Visage Imaging, Inc.) upon thresholding the image stack such that the airways were transparent and the tissues opaque.

To retrieve quantitative information from the in-focus interface, a line profile across a major airway shown in figure 5(a) is plotted in figure 5(b). Here the distribution of the refractive index decrement averages around the expected value listed in table 1. Also, a line profile is plotted across the magnified (blurred) bone feature seen in figure 5(c), which helps us to observe the over-smoothing of the bone/soft-tissue interface and the quantitatively incorrect reconstruction of δ (see table 1).

We note here that other soft tissues can be seen as amorphous shapes surrounding the chest wall in the phase retrieved reconstruction in figure 4(a). These tissues are more evident than in the raw reconstruction in figure 3(b). We attribute this increased clarity to the shape of the Fourier filter required for the lung tissue/air interface used in equation (1) being likely very similar to that used in equation (2) that would be used to focus on soft-tissue interfaces.

To focus on the bone/lung tissue interface, we instead process every image with equation (2) before tomographically reconstructing each slice. To apply this equation, we use the δ and μ values for bone as well as those for water together with *a priori* knowledge of the total projected thickness $A(\mathbf{r}_\perp)$. $A(\mathbf{r}_\perp)$ is required to determine the attenuation that the object would provide if it were made entirely of a single homogenous material, which is used in the normalization term $I_0 \exp[-\mu_1 A(\mathbf{r}_\perp)]$ of equation (2). Here we have approximated the normalization term by fitting a parabolic curve to the intensity profile at each projection. This only works well since the animal was inside a water-filled cylinder and because the lungs are approximately circular in projection and were located near the centre of the tube. Although this approximation will reduce the accuracy of the reconstruction, we see no artefacts in the resulting reconstruction, justifying its use.

In figure 6(a), a tomographic reconstruction of the same slice as in figures 3(b) and 4(a) is shown, which now focuses on the bone/lung tissue interfaces. From this image, we see that the interfaces of interest have now been correctly reconstructed, yielding a sharp boundary between the media. This can be better appreciated in figure 6(b), which shows the same zoomed-in region as in figure 4(c) but now the boundaries and features are highly visible. Additionally, the line profile in figure 6(c) shows the quantitative measure of the refractive index decrement, δ . The large fluctuations in δ arise from the porosity of the bone, but the maximum value underestimates the expected value from table 1. We believe that this discrepancy arises because the tabulated values are calculated for mature, fully calcified bone, whilst the immature bones of the newborn rabbit will differ considerably in their average density and composition (i.e. not be fully calcified), compared to those of an adult rabbit, thereby lowering the measured δ value.

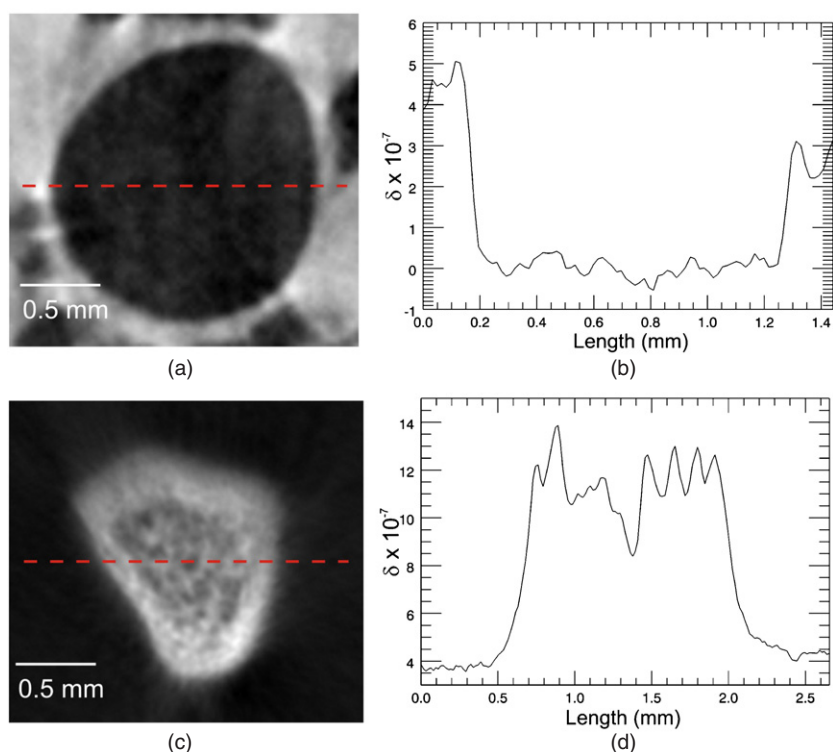


Figure 5. (a) Magnified region of figure 4(a) showing a major airway. Its line profile is plotted from left to right from the centre of the image and is shown in (b) displaying the distribution of its refractive index decrement. (c) The same image as in figure 4(c) with its line profile shown in (d).

To compare the improvement in the SNR before and after the phase retrieval for the bone/tissue interface, we observed the cortical bone (outer edge) of the bone segment seen in figure 6(c). The cortical bone contains fewer pores than the internal trabecular bone and enables comparison against the raw image far from phase-contrast fringes (i.e. a measure of approximately pure attenuation by bone). We measured the mean signal within small areas of cortical bone and measured the noise from the nearby soft tissue that was also free of phase-contrast effects. For bone, the SNR in the raw ‘absorption-contrast’ image was only 5 ± 1 compared to the same area in the phase retrieved image with an SNR of 47 ± 12 . On average, we found an improvement in the SNR of 9 ± 3 times afforded by phase retrieval. Whilst this is less than the improvement seen for the soft-tissue reconstruction, this results from the reduced level of spatial filtering in equation (2) due to the reduced phase gradients present at the bone/tissue interface compared to the air/tissue interface.

Finally, we draw attention to the air/lung tissue interfaces in figure 6(a), which have now been over-sharpened, or insufficiently filtered, by the phase retrieval process resulting from under-compensation of the phase-contrast fringes. Therefore, the air/tissue interfaces have been incorrectly reconstructed.

Upon reconstructing all interfaces of interest, we now combine the images in figures 4(a) and 6(a) to compose a spliced reconstruction (figure 7). To produce the spliced image, one cannot simply manually insert the appropriate region into the corresponding regions of another image. We began by using the soft-tissue image (figure 4) and exploited the fact that the relatively highly attenuating bones appear blurred, realizing that the true bone interfaces

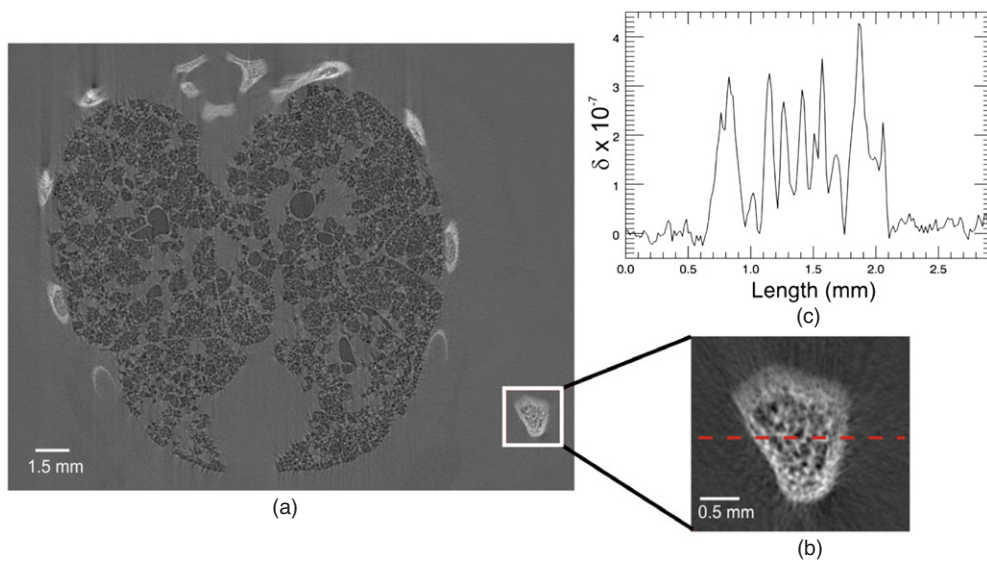


Figure 6. (a) Interface-specific tomographic reconstruction of a preterm rabbit pup thorax, focusing on the bone/lung tissue interface. (b) Magnified section of (a) which now shows a sharp and quantitative reconstruction of the same images seen in figures 4(c) and 5(c). (c) Line profile from left-to-right across the centre of (b) showing the distribution of the refractive index decrement of the porous bone.

must lie within those blurred regions. The large contrast enabled the image to be thresholded until the blurred bones were invisible, thereby creating a binary ‘soft-tissue-only’ mask. The inverse of this mask was then applied to the image containing the correctly reconstructed bones (figure 6). By smoothing each binary mask, and ensuring both masks summed to unity before multiplying with the relevant image, a continuous and smooth spliced image was formed by adding the masked images together. One additional step involved adjusting any offsets so that the background encasing material had the same average value in each image before creating the spliced image.

The spliced image shows all interfaces both quantitatively and sharply reconstructed, which demonstrates the key result that we are able to perform phase and amplitude tomography of multi-material objects that are spatially quantized with only one PBI image per tomographic orientation.

One drawback of our image splicing is that the objects in question should be spatially separated by an amount equal to the bleeding (pollution length) associated with over-smoothing the second interface. In Beltran *et al* (2010), it was shown that this bleed width (Δx) depends only on the refractive index of the encasing material, where $\Delta x \geq \sqrt{d\delta_1/\mu_1}$. It was experimentally verified that a distance of three to five times Δx was sufficient to avoid locally polluting nearby objects of a different refractive index. For our experiment, this distance should therefore be at least $180 \mu\text{m}$, but no more than $300 \mu\text{m}$. This reduces the accuracy of the reconstruction where the bone encroaches on the airways. Fortunately, we see very little evidence of the contamination between media in the spliced reconstruction of figure 7.

4.2. Brain imaging

Figure 8(a) shows a single PBI image from the CT dataset of a rat brain prepared as described in section 3.3. Due to the similar complex refractive indices of brain and agar (table 2), the

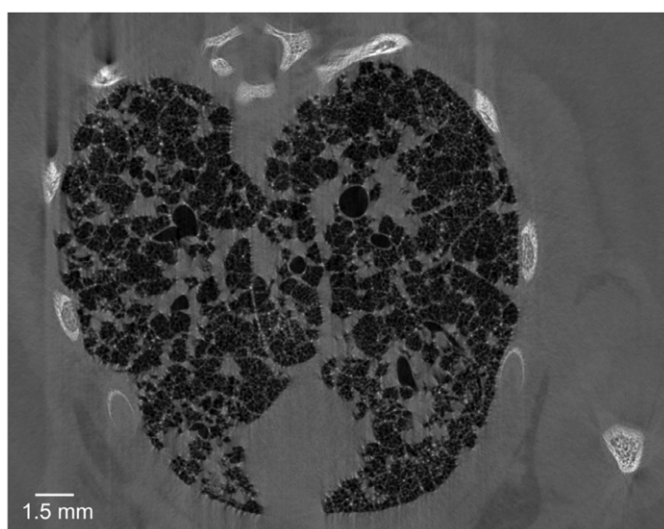


Figure 7. Spliced tomographic reconstruction of preterm rabbit pup lungs, constructed by splicing figures 4(a) and 6(a).

brain is not visible in a single projection image even with the very long propagation distance of 5.0 m. However, if we apply filtered backprojection directly to the set of raw PBI brain images (figure 8(b)), a small amount of anatomical detail becomes visible and structures are resolved relative to the gel agar matrix. This is principally due to the averaging effect caused by acquiring images from multiple projections which improves the SNR. Figure 8(b) shows a single tomographic slice in a para-frontal orientation at an approximate anterior–posterior distance of 9.4 mm caudal to bregma. The bright white flares seen in the image are possibly caused by attenuation due to Bragg diffraction from crystallite regions in the agar matrix.

Phase retrieval was then applied before performing the tomographic reconstruction. As described above, all materials in the brain sample effectively refract and attenuate x-rays to a similar degree; hence, the sample behaves somewhat like a single-material object and thus we need to utilize equation (1) only (see figure 2). We used the δ and μ values for grey/white matter listed in table 2. The same slice in figure 8(b) is shown in figure 9, now with the phase retrieval process included. Despite the subtle differences in complex refractive index, the tomogram yields clearly demarcated tissue borders at the grey/white matter boundaries. Considerable detail can be seen in the brainstem, including the ventral cochlear nucleus (vCN), spinal tract of the trigeminal nerve (TST) and inferior cerebellar peduncle (iCP).

SNR values were calculated for six 30×30 pixel regions of grey or white matter in both figures 8(b) and 9 yielding values of 2.1 ± 0.2 and 440 ± 120 , respectively. Again we note that the regions selected for the calculations did not contain any phase-contrast signal. For brain imaging with this geometry, we found a net gain in the SNR of 200 ± 50 over absorption contrast. This exceptional improvement is a consequence of the relatively large propagation distance of 5.0 m used to render the brain visible, which translates to heavy spatial filtering (see figure 2) and associated strong noise suppression in the phase retrieval step (equation (1)); this effect was also discussed by Arhatari *et al* (2010). Note that if one were to use too large a propagation distance, the validity conditions of the underlying transport-of-intensity equation would be violated.

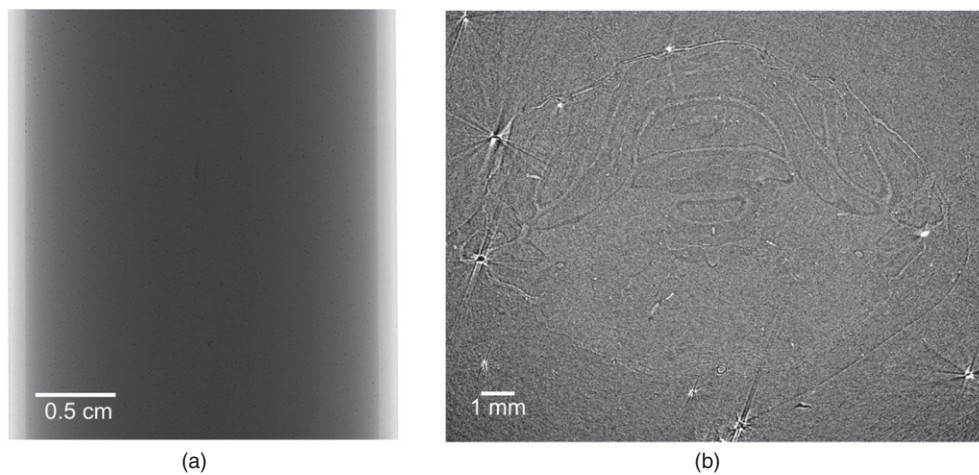


Figure 8. (a) PBI image of an excised rat brain submerged in an agar solution. X-ray energy = 24 keV, propagation distance = 5.0 m. (b) Tomographic reconstruction of a single slice from the raw brain PBI images using filtered backprojection.

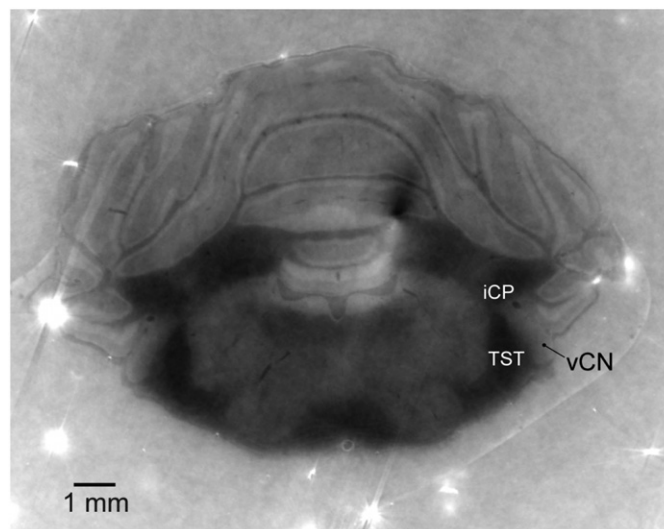


Figure 9. Tomographic reconstruction of the same slice as shown in figure 8(b). Equation (1) was applied to each image before tomographically reconstructing.

Phase-contrast modalities that are more sensitive to weak phase gradients, such as grating interferometry, can render visible the tissues of the brain with even higher contrast than that presented above (Pfeiffer *et al* 2007). However, the extra sensitivity of such methods makes them less robust for imaging objects that also contain strong phase gradients such as the air/soft-tissue boundaries within the lung. Moreover, phase retrieval in that context requires multiple images to be acquired for every projection (Pfeiffer *et al* 2007), thereby significantly increasing the x-ray dose to the sample. The benefits of our approach include the simple imaging geometry, with no requirement for post-sample optical elements, and only a single exposure per projection required for phase retrieval.

5. Future work

A key finding of this study was that the single-material phase retrieval algorithm (equation (1)) was sufficiently suitable for the sample containing brain tissue (containing both grey and white matter) in agar. This considerably simplified and sped up the analysis as only a single tomographic reconstruction was required. It remains to be seen whether other material combinations, including soft tissues, can be analysed in the same way. For example, it may be valid to make the single-material approximation in a sample exclusively comprised of soft tissues. It also remains to be seen whether a clear image of the brain can be reconstructed when the brain is *in situ*, inside the skull, using either phase retrieval algorithm.

With a view to ultimately applying our method to laboratory-based PBI using polychromatic radiation (e.g., Wilkins *et al* 1996), it would be very useful to generalize it to a polychromatic spectrum. This will be a stepping stone allowing the technique to be used for routine biomedical imaging, with potential clinical implications since PBI is already being used in the clinic for breast imaging (Tanaka *et al* 2005). We note that several groups have made inroads into the problem of phase retrieval using polychromatic radiation in the contexts of both two- and three-dimensional imaging (Arhatari *et al* 2005, Myers *et al* 2007).

Also, we note that spatially quantized objects are in some sense sparse, insofar as the interfaces between the various volumetric regions of the object are intrinsically two-dimensional surfaces. No attempt has been made to utilize this sparseness in this paper. Progress has been made in using the intrinsically sparse nature of spatially quantized objects in the context of phase retrieval in the work of Myers *et al* (2008a, 2008b, 2010) and the work on gradient-sparse objects by Sidky *et al* (2010). Furthermore, the burgeoning field of compressive sensing (Baraniuk 2007) has also made inroads into the tomography of sparse objects, albeit via a different form of sparsity in which the majority of features in the object are confined to a small fraction of the volume occupied by the object. It might be interesting to investigate whether these methods of compressive sensing may be adapted to spatially quantized objects, in which the volume occupied by *interfaces* is sparse (cf Sidky *et al* 2010). In this context, the concept of a quasi-one-dimensional object, developed by Gureyev and Evans (1998), might also prove useful. A particular driver is the quest to reduce the number of required projections (and therefore the dose to the sample) by making use of the sparseness of interface-occupying voxels in a typical spatially quantized object.

6. Conclusions

We have demonstrated that interface-specific x-ray phase retrieval tomography, using the method developed by Beltran *et al* (2010), can be performed on complex biological objects. The method makes use of only a single PBI image per tomographic orientation and requires *a priori* information of the sample's total projected thickness at each orientation and knowledge of each material's complex refractive index present in the sample. Note that for a sample containing no internal voids, the total projected thickness at each orientation is completely determined by knowledge of the surface of the object. The method was successfully implemented on experimental propagation-based phase-contrast tomographic data of the thorax and brain of small animals collected using x-ray synchrotron radiation. For the thorax data, quantitative reconstructions of air/lung tissue and bone/lung tissue interfaces were performed separately and were then spliced together to yield a complete reconstruction. A tomographic reconstruction of a rat brain was made under the assumption that it comprised of a single material of variable density, which resulted in an image able to clearly distinguish between grey and white matter. SNR calculations were carried out and showed our technique

to be superior to conventional absorption contrast by factors ranging from 9 to 200 fold. This gain depended on the material in question and the experimental setup, but can potentially be traded against a reduction in x-ray dose. This enhances the dose reduction already made over other implementations of phase retrieval since only a single image per projection is required. Given these results, combined with the simplicity of our technique, we anticipate that it will potentially be a useful tool in the field of biomedical x-ray imaging.

Acknowledgments

The authors would like to thank Kaye Morgan for assisting us in producing the supplementary online movie (available at stacks.iop.org/PMB/56/7353/mmedia) and to Kentaro Uesugi for helping set up the experiments. MAB acknowledges funding from the Monash University Dean's Scholarship Scheme. DMP acknowledges funding from the Australian Research Council (ARC). MJK is an ARC Australian Research Fellow. SBH is a NHMRC Principal Research Fellow. This research was partially funded by the Victorian Government's Operational Infrastructure Support Program. We acknowledge travel funding provided by the International Synchrotron Access Program (ISAP) managed by the Australian Synchrotron and Funded by the Australian Government.

References

- Anastasio M A and Pan X 2000 Computationally efficient and statistically robust image reconstruction in three-dimensional diffraction tomography *J. Opt. Soc. Am. A* **17** 391–400
- Anastasio M A, Shi D, De Carlo F and Pan X 2004 Analytic image reconstruction in local phase-contrast tomography *Phys. Med. Biol.* **49** 121–44
- Arhatari B D, Gates W P, Eshtiaghi N and Peele A G 2010 Phase retrieval tomography in the presence of noise *J. Appl. Phys.* **107** 034904
- Arhatari B D, Nugent K A, Peele A G and Thornton J 2005 Phase contrast radiography: II. Imaging of complex objects *Rev. Sci. Instrum.* **76** 113704
- Baraniuk R G 2007 Compressive sensing *IEEE Signal Process. Mag.* **24** 118–21
- Beltran M A, Paganin D M, Uesugi K and Kitchen M J 2010 2D and 3D x-ray phase retrieval of multi-material objects using a single defocus distance *Opt. Express* **18** 6423–36
- Bronnikov A V 2002 Theory of quantitative phase-contrast computed tomography *J. Opt. Soc. Am. A* **19** 472–80
- Cloetens P, Barrett R, Baruchel J, Guigay J-P and Schlenker M 1996 Phase objects in synchrotron radiation hard x-ray imaging *J. Phys. D: Appl. Phys.* **29** 133–46
- Cloetens P, Ludwig W, Baruchel J, van Dyck D, van Landuyt J, Guigay J P and Schlenker M 1999 Holotomography: quantitative phase tomography with micrometer resolution using hard synchrotron radiation x-rays *Appl. Phys. Lett.* **75** 2912–4
- Cloetens P, Pateyron-Salomé M, Buffière J Y, Peix G, Baruchel J, Peyrin F and Schlenker M 1997 Observation of microstructure and damage in materials by phase sensitive radiography and tomography *J. Appl. Phys.* **81** 5878–86
- Förster E, Goetz K and Zaumseil P 1980 Double crystal diffractometry for the characterization of targets for laser fusion experiments *Krist. Tech.* **15** 937–45
- Goto S *et al* 2001 Construction and commissioning of a 215 m-long beamline at SPring-8 *Nucl. Instrum. Methods A* **467** 682–5
- Guigay J P, Langer M, Renaud B and Cloetens P 2007 Mixed transfer function and transport of intensity approach for phase retrieval in the Fresnel region *Opt. Lett.* **32** 1617–9
- Gureyev T E and Evans R 1998 An extension of quasi-one-dimensional tomography *Appl. Opt.* **37** 2628–36
- Gureyev T E, Nesterets Y I and Mayo S C 2007 Quantitative quasi-local tomography using absorption and phase contrast *Opt. Commun.* **280** 39–48
- Gureyev T E and Nugent K A 1996 Phase retrieval with the transport-of-intensity equation: II. Orthogonal series solution for nonuniform illumination *J. Opt. Soc. Am. A* **13** 1670–82
- Gureyev T E and Nugent K A 1997 Rapid quantitative phase imaging using the transport of intensity equation *Opt. Commun.* **133** 339–46
- Gureyev T E, Paganin D M, Myers G R, Nesterets Y I and Wilkins S W 2006 Phase-and-amplitude computer tomography *Appl. Phys. Lett.* **89** 034102

- Hooper S B *et al* 2007 Imaging lung aeration and lung liquid clearance at birth *FASEB J.* **21** 3329–37
- Irvine S C, Paganin D M, Dubsky W, Lewis R A and Fouras A 2008 Phase retrieval for improved three-dimensional velocimetry of dynamic x-ray blood speckle *Appl. Phys. Lett.* **93** 153901
- Kak A C and Slaney M 1988 *Principles of Computerized Tomographic Imaging* (New York: IEEE)
- Kitchen M J *et al* 2008 Dynamic measures of regional lung air volume using phase contrast x-ray imaging *Phys. Med. Biol.* **53** 6065–77
- Kitchen M J, Habib A, Fouras A, Dubsky S, Lewis R A, Wallace M J and Hooper S B 2010 A new design for high stability pressure-controlled ventilation for small animal lung imaging *J. Instrum.* **5** T02002
- Kitchen M J, Paganin D, Lewis R A, Yagi N, Uesugi K and Mudie S T 2004 On the origin of speckle in x-ray phase contrast images of lung tissue *Phys. Med. Biol.* **49** 4335–48
- Mayo S C, Davis T J, Gureyev T E, Miller P R, Paganin D, Pogany A, Stevenson A W and Wilkins S W 2003 X-ray phase-contrast microscopy and microtomography *Opt. Express* **11** 2289–302
- McMahon P J, Peele A G, Paterson D, Lin J J A, Irving T H K, McNulty I and Nugent K A 2003 Quantitative x-ray phase tomography with sub-micron resolution *Opt. Commun.* **217** 53–8
- Momose A, Takeda T, Itai Y and Hirano K 1996 Phase-contrast x-ray computed tomography for observing biological soft tissues *Nat. Med.* **2** 473–5
- Myers G R, Gureyev T E, Paganin D M and Mayo S C 2008a The binary dissector: phase contrast tomography of two- and three- material objects from few projections *Opt. Express* **16** 16736–49
- Myers G R, Mayo S C, Gureyev T E, Paganin D M and Wilkins S W 2007 Polychromatic cone-beam phase-contrast tomography *Phys. Rev. A* **76** 045804
- Myers G R, Paganin D M, Gureyev T E and Mayo S C 2008b Phase-contrast tomography of single-material objects from few projections *Opt. Express* **16** 908–19
- Myers G R, Thomas C D L, Paganin D M, Gureyev T E and Clement J G 2010 A general few-projection method for tomographic reconstruction of samples consisting of several distinct materials *Appl. Phys. Lett.* **96** 021105
- Paganin D, Gureyev T E, Mayo S C, Stevenson A W, Nesterets Y A I and Wilkins S W 2004 X-ray omni microscopy *J. Microsc.* **214** 315–27
- Paganin D, Mayo S C, Gureyev T E, Miller P R and Wilkins S W 2002 Simultaneous phase and amplitude extraction from a single defocused image of a homogeneous object *J. Microsc.* **206** 33–40
- Paganin D and Nugent K A 1998 Noninterferometric phase imaging with partially coherent light *Phys. Rev. Lett.* **80** 2586–9
- Pellegrino L J, Pellegrino A S and Cushman A J 1979 *A Stereotaxic Atlas of the Rat Brain* (New York: Plenum)
- Pfeiffer F, Bunk O, David C, Bech M, Le Duc G, Bravin A and Cloetens P 2007 High-resolution brain tumor visualization using three-dimensional x-ray phase contrast tomography *Phys. Med. Biol.* **52** 6923–30
- Pogany A, Gao D and Wilkins S W 1997 Contrast and resolution in imaging with a microfocus x-ray source *Rev. Sci. Instrum.* **68** 2774–82
- Saleh B E A and Teich M C 1991 *Fundamentals of Photonics* (Toronto: Wiley)
- Shi D, Anastasio M A and Pan X 2005 Reconstruction of refractive index discontinuities from truncated phase-contrast tomography projections *Appl. Phys. Lett.* **86** 034102
- Sidky E Y, Anastasio M A and Pan X 2010 Image reconstruction exploiting object sparsity in boundary-enhanced x-ray phase-contrast tomography *Opt. Express* **18** 10404–22
- Snigirev A, Snigireva I, Kohn V, Kuznetsov S and Schelokov I 1995 On the possibilities of x-ray phase contrast microimaging by coherent high-energy synchrotron radiation *Rev. Sci. Instrum.* **66** 5486–92
- Stevenson A W, Mayo S C, Häusermann D, Maksimenko A, Garrett R F, Hall C J, Wilkins S W, Lewis R A and Myers D E 2010 First experiments on the Australian synchrotron imaging and medical beamline, including investigations of the effective source size in respect of x-ray imaging *J. Synchrotron Radiat.* **17** 75–80
- Stock S R (ed) 2010 *Developments in X-Ray Tomography VII, Proc. SPIE* **7804** http://spie.org/x648.html?product_id=850961
- Suzuki Y, Yagi N and Uesugi K 2002 X-ray refraction-enhanced imaging and a simple method for phase retrieval for a simple object *J. Synchrotron Radiat.* **9** 160–5
- Tanaka T *et al* 2005 The first trial of phase contrast imaging for digital full-field mammography using a practical molybdenum x-ray tube *Invest. Radiol.* **40** 385–96
- Teague M R 1983 Deterministic phase retrieval: a Green's function solution *J. Opt. Soc. Am.* **73** 1434–41
- Turner D, Weber K P, Paganin D and Scholten R E 2004 Off-resonant defocus-contrast imaging of cold atoms *Opt. Lett.* **29** 232–4
- Wilkins S W, Gureyev T E, Gao D, Pogany A and Stevenson A W 1996 Phase-contrast imaging using polychromatic hard x-rays *Nature* **384** 335–8
- Wolf E 1969 Three-dimensional structure determination of semi-transparent objects from holographic data *Opt. Commun.* **1** 153–6